Velocity moments in alongshore bottom stress parameterizations

Falk Feddersen and R.T. Guza

Center for Coastal Studies, Scripps Institution of Oceanography, University of California San Diego
La Jolla, California

Steve Elgar

Woods Hole Oceanographic Institution, Woods Hole, Massachusetts

T.H.C. Herbers

Department of Oceanography, Naval Postgraduate School, Monterey, California

Abstract. The time-averaged alongshore bottom stress is an important component of nearshore circulation models. In a widely accepted formulation the bottom stress is proportional to $< |\vec{u}|v >$, the time average of the product of the instantaneous velocity magnitude $|\vec{u}|$ and the instantaneous alongshore velocity component v. Both mean and fluctuating (owing to random, directionally spread waves) velocities contribute to $< |\vec{u}|v >$. Direct estimation of $< |\vec{u}|v >$ requires a more detailed specification of the velocity field than is usually available, so the term $< |\vec{u}|v >$ is parameterized. Here direct estimates of $< |\vec{u}|v >$ based on time series of near-bottom currents observed between the shoreline and 8-m water depth are used to test the accuracy of $< |\vec{u}|v >$ parameterizations. Common $< |\vec{u}|v >$ parameterizations that are linear in the mean alongshore current significantly underestimate $< |\vec{u}|v >$ for moderately strong alongshore currents, resulting in overestimation of a drag coefficient determined by fitting modeled (with a linearized bottom stress) to observed alongshore currents. A parameterization based on a joint-Gaussian velocity field with the observed velocity statistics gives excellent overall agreement with the directly estimated $< |\vec{u}|v >$ and allows analytic investigation of the statistical properties of the velocity field that govern $< |\vec{u}|v >$. Except for the weakest flows, $< |\vec{u}|v >$ depends strongly on the mean alongshore current and the total velocity variance but depends only weakly on the mean wave angle, wave directional spread, and mean cross-shore current. Several other nonlinear parameterizations of $< |\vec{u}|v >$ are shown to be more accurate than the linear parameterizations and are adequate for many modeling purposes.

1. Introduction

The time-averaged alongshore bottom stress τ_y^b plays a crucial role in the dynamics of mean alongshore currents in the nearshore. A commonly used stress formulation is [e.g., *Longuet-Higgins*, 1970; *Grant and Madsen*, 1979; *Battjes*, 1988; *Garcez-Faria et al.*, 1998; *Feddersen et al.*, 1998]

$$\tau_y^b = \rho c_f < |\vec{u}|v >, \qquad (1)$$

where $< \cdot >$ represents a time average over many wave periods, ρ is the water density, and c_f is a nondimensional drag coefficient. The total instantaneous horizontal velocity vector $|\vec{u}|$ and the instantaneous alongshore velocity v are evaluated near the seafloor but above the bottom boundary layer. Mean and fluctuating velocity components contribute to the nonlinear term $< |\vec{u}|v >$.

Although the stress form (1) is widely accepted, the term $< |\vec{u}|v >$ usually is parameterized in nearshore circulation models because estimation of $< |\vec{u}|v >$ requires detailed specification of the fluctuating velocity field over a broad range of timescales (e.g., sea, swell, infragravity, and shear waves). Analogous parameterizations are necessary in other oceanographic contexts, including mean flow in the presence of tidal currents [*Bowden*, 1953] and large-scale ocean circulation [*Rooth*, 1972].

Here several linear and nonlinear parameterizations of $< |\vec{u}|v >$ widely used in nearshore circulation models (reviewed in section 2) are tested with an extensive field data set described in section 3. The $< |\vec{u}|v >$ term is calculated directly from the observed velocity time series and compared with parameterizations based on velocity statistics estimated from the same observations. The bottom stress is also a function of c_f (1), and c_f may depend on the flow environment, the elevation above the bed where $< |\vec{u}|v >$ is evaluated, and the bottom roughness [e.g., *Grant and Madsen*, 1979; *Garcez-Faria et al.*, 1998]. The dependence of c_f on these factors is not investigated here.

As discussed in section 4, parameterizations linear in the mean alongshore current often are inaccurate because the underlying assumptions (e.g., weak-currents) are violated. Estimates of $< |\vec{u}|v >$ based on the assumption of an isotropic Gaussian velocity field [*Wright and Thompson*, 1983] are generalized to a joint-Gaussian velocity field corresponding to arbitrary wave-directional distributions. Although this accurate parameterization requires a more detailed specification of velocity field statistics than is generally available, it enables identification of the nondimensional variables controlling $< |\vec{u}|v >$, providing a basis for further simplification. Several existing nonlinear parameterizations and special cases of the joint-Gaussian parameterization are found to be accurate. The mean alongshore current and total velocity variance are the components critical to parameterizing $< |\vec{u}|v >$ well. The consequences of neglecting infragravity (< 0.05 Hz) velocity fluctuations in $< |\vec{u}|v >$ and of using different parameterizations of $< |\vec{u}|v >$ in a simple alongshore current model are discussed in section 5. Results are summarized in section 6.

2. The $< |\vec{u}|v >$ Parameterizations

The weak current, small angle parameterization of $< |\vec{u}|v >$ is linear in the mean alongshore current and therefore often is used in models of surf zone circulation [e.g., *Wu et al.*, 1985; *Özkan-Haller and Kirby*, 1999]. The cross-shore u and alongshore v velocities are decomposed into mean and fluctuating components (e.g., $u = \overline{u} + u'$), with variances σ_u^2 and σ_v^2, respectively. The total velocity variance $\sigma_T^2 = \sigma_u^2 + \sigma_v^2$. Assuming $\overline{u} = 0$, and applying the weak-current ($|\overline{v}| \ll \sigma_T$) and small-angle ($\sigma_v \ll \overline{v}$) approximations yields

$$< |\vec{u}|v >=< |u'| > \overline{v}. \tag{2}$$

For monochromatic and unidirectional waves with period T (radian frequency ω) and wave velocity amplitude u_0 propagating at small angle θ relative to normal incidence (e.g., $u' = u_0 \cos(\theta) \cos(\omega t)$), (2) yields [*Longuet-Higgins*, 1970; *Thornton*, 1970]

$$\begin{aligned} < |\vec{u}|v > &= < |u'| > \overline{v} = u_0 \overline{v} \cdot \frac{1}{T} \int_T |\cos(\omega t)| dt \\ &= \frac{2}{\pi} u_0 \overline{v} = \frac{2\sqrt{2}}{\pi} \sigma_T \overline{v}. \end{aligned} \tag{3}$$

Thornton and Guza [1986] extended (2) to unidirectional waves with a narrow frequency spectrum and Rayleigh distributed u_0 [*Longuet-Higgins*, 1952] with probability density function

$$P(u_0) = \frac{u_0}{\sigma_T^2} \exp\left(-\frac{u_0^2}{2\sigma_T^2}\right). \tag{4}$$

Using (4) in (2) yields

$$\begin{aligned} < |u'| > \overline{v} &= E[|u'|]\overline{v} = \overline{v} \int_0^\infty u_0 P(u_0) du_0 \\ &\times T^{-1} \int_T |\cos(\omega t)| dt = \sqrt{\frac{2}{\pi}} \sigma_T \overline{v} \\ &= 0.798 \sigma_T \overline{v} \end{aligned} \tag{5}$$

where $E[\cdot]$ is the expected value. Note that (5) can also be derived from the less restrictive assumption of Gaussian-distributed wave orbital velocities [*Longuet-Higgins*, 1952], that is,

$$\begin{aligned} < |u'| > \overline{v} &= \frac{\overline{v}}{\sqrt{2\pi}\sigma_T} \int_{-\infty}^\infty |u'| \exp\left(\frac{-u'^2}{2\sigma_T^2}\right) du' \\ &= \sqrt{\frac{2}{\pi}} \sigma_T \overline{v}. \end{aligned}$$

Other weak-current linearized forms for $< |\vec{u}|v >$ follow from different assumptions about the fluctuating velocity field. For example, *Liu and Dalrymple* [1978] relaxed the small–angle assumption used in (3) and showed (for monochromatic waves) that

$$< |\vec{u}|v >= \frac{2\sqrt{2}}{\pi} \sigma_T \overline{v} (1 + \sin^2 \theta). \tag{6}$$

Wave obliquity thus increases $< |\vec{u}|v >$ relative to small angles (3).

Rayleigh friction,

$$< |\vec{u}|v >= \mu \overline{v}, \tag{7}$$

where μ is a constant dimensional drag coefficient, has been used in models of surf zone alongshore currents [*Bowen*, 1969], shear waves [e.g., *Dodd et al.*, 1992; *Allen et al.*, 1996; *Slinn et al.*, 1998; *Feddersen*, 1998], and shelf circulation [e.g., *Lentz and Winant*, 1986; *Lentz et al.*, 1999]. Rayleigh friction follows from assuming a constant σ_T in (5).

Ebersole and Dalrymple [1980] introduced a general formulation for linear, unidirectional, monochromatic waves. With $\overline{u} = 0$, the result (hereinafter ED80) is

$$\begin{aligned} < |\vec{u}|v > &= T^{-1} \int_T [u_0^2 \cos^2(\omega t) + 2\overline{v}u_0 \sin(\theta) \cos(\omega t) \\ &+ \overline{v}^2]^{1/2} [\overline{v} + u_0 \sin(\theta) \cos(\omega t)] dt. \end{aligned} \tag{8}$$

Thornton and Guza [1986] extended ED80 to a narrow-frequency spectrum. Evaluating (8) for each orbital wave velocity amplitude u_0 gives $\overline{|\vec{u}|v}(u_0)$, and integrating over the Rayleigh probability density function $P(u_0)$ (4) yields (hereinafter TG86)

$$< |\vec{u}|v >= E[\overline{|\vec{u}|v}(u_0)] = \int_0^\infty \overline{|\vec{u}|v}(u_0) \cdot P(u_0) du_0. \tag{9}$$

Both ED80 and TG86 are nonlinear in $\overline{v}$ and must be integrated numerically.

On a planar beach with maximum observed alongshore current $\overline{v}_{max} \approx 0.6$ m/s, *Thornton and Guza* [1986] showed that one-dimensional (1-D) model solutions with linear (5) and nonlinear TG86 (9) parameterizations both approximately reproduce the observed cross-shore variation of $\overline{v}(x)$. However, the best fit values of the drag coefficient c_f with TG86 was 0.6 to 0.8 of the c_f using (5). *Thornton and Guza*

[1986] suggest the c_f values differed because $|\bar{v}|/\sigma_T$ was $O(1)$, violating the weak-current assumption underlying (5). On a barred beach with stronger $\bar{v}_{max} \approx 1.5$ m/s, $\bar{v}(x)$ solutions with (5) and with TG86 differ substantially, even using c_f values that yield the same modeled $\bar{v}_{max}$ [*Church and Thornton*, 1993]. In this case, the weak-current assumption likely was violated more severely than the cases with weaker $\bar{v}_{max}$ considered by *Thornton and Guza* [1986]. These differences suggest that the weak-current linearized parameterization (5) is inaccurate. Although weak currents and small angles are not assumed in ED80 and TG86, the mean cross-shore current and directional spreading of waves are neglected, introducing errors that are not understood well.

Wright and Thompson [1983] investigated the accuracy of the linearized parameterization in the special case of an isotropic ($\sigma_u = \sigma_v = \sigma_T/\sqrt{2}$), uncorrelated Gaussian fluctuating velocity field, where

$$< |\vec{u}|v > = E[|\vec{u}|v] = \int\!\!\!\int_{-\infty}^{\infty} (u'^2 + v'^2 + 2\bar{v}v' + \bar{v}^2)^{1/2}$$
$$\times \; (\bar{v} + v')P(u',v')du'dv', \qquad (10)$$

with the probability density function

$$P(u',v') = \frac{1}{2\pi\sigma_u^2} \exp\left[-\frac{1}{2\sigma_u^2}(u'^2 + v'^2)\right].$$

Although $< |\vec{u}|v >$ is a function of two parameters, $\bar{v}$ and σ_T, the ratio $< |\vec{u}|v > /\sigma_T\bar{v}$ is a function of only $|\bar{v}|/\sigma_T$. Integrating (10) numerically, *Wright and Thompson* [1983] showed that for $0 < |\bar{v}|/\sigma_T \leq 1$, $< |\vec{u}|v > /\sigma_T\bar{v}$ is relatively constant and varies by 23% from its weak-current value of $0.75\sqrt{\pi} = 1.33$. Note that the small-angle random wave weak-current limit is 0.798. *Wright and Thompson* [1983] showed that the ratio $< |\vec{u}|v > /\sigma_T\bar{v}$ for an isotropic, uncorrelated Gaussian velocity field is represented well (maximum error of 2%) for all values of $|\bar{v}|/\sigma_T$ by an empirical form (hereinafter WT83)

$$\frac{< |\vec{u}|v >}{\sigma_T\bar{v}} = \left[\alpha^2 + (\bar{v}/\sigma_T)^2\right]^{1/2}, \qquad (11)$$

with $\alpha = 1.33$. WT83 has the correct strong current limit $|\bar{v}|\bar{v}$ and the correct weak-current limit for an isotropic wave field.

Naturally occurring wave-induced velocity fields are neither unidirectional nor isotropic. The formulation of *Wright and Thompson* [1983] is generalized here to include velocity fluctuations with arbitrary directional distributions by assuming u and v are joint-Gaussian distributed random variables

$$E[|\vec{u}|v] = \int\!\!\!\int_{-\infty}^{\infty} (u^2 + v^2)^{1/2}vP(u,v)dudv. \qquad (12)$$

The joint probability density function $P(u,v)$, given in Appendix A, is a function of $\bar{u}$, $\bar{v}$, σ_u, σ_v, and the correlation coefficient ρ_{uv},

$$\rho_{uv} = \frac{<u'v'>}{\sigma_u\sigma_v}.$$

The velocity moments σ_u, σ_v, and ρ_{uv} are related to the mean angle $\bar{\theta}$ and spread σ_θ for a directionally distributed wave field [*Kuik et al.*, 1988; *Herbers et al.*, 1999]. A unidirectional wave field corresponds to $\sigma_\theta^2 = 0$, $|\rho_{uv}| = 1$, and $\tan(|\bar{\theta}|) = \sigma_v/\sigma_u$, an isotropic wave field corresponds to $\rho_{uv} = 0$ and $\sigma_v = \sigma_u$, and a wave field spread symmetrically about normal incidence ($\bar{\theta} = 0$) corresponds to $\rho_{uv} = 0, \sigma_v \neq 0$, and

$$\sigma_\theta^2 = \frac{\sigma_v^2}{\sigma_u^2 + \sigma_v^2}.$$

In general, (12) must be evaluated numerically (Appendix A). Special cases depend on fewer variables and are easier to evaluate. When $|\rho_{uv}| = 1$ (i.e., $\sigma_\theta = 0$, a unidirectional assumption similar to TG86), the double integral (12) collapses to a single integral (A4). For small angles ($\sigma_v = 0$) and $\bar{u} = 0$, a closed form solution exists (Appendix C, hereinafter SA).

$E[|\vec{u}|v]/\sigma_T\bar{v}$ is a function of four nondimensional parameters ($\bar{v}/\sigma_T$, $\bar{u}/\sigma_T$, σ_v/σ_u, and ρ_{uv}; Appendix B). Weak-currents ($|\bar{v}|/\sigma_T \ll 1$) and $\bar{u}/\sigma_T = 0$ result in $E[|\vec{u}|v]/\sigma_T\bar{v} = \alpha(\sigma_v/\sigma_u, \rho_{uv})$ (B4), a function of two parameters (equivalent to $\bar{\theta}$ and σ_θ). For unidirectional waves ($|\rho_{uv}| = 1$), the closed form expression (B5) shows that the increase in $< |\vec{u}|v > /\sigma_T\bar{v} = \alpha(\sigma_v/\sigma_u)$ owing to wave obliquity is $1 + \sin^2\theta$, similar to the dependence for monochromatic waves (6). As $\theta \to 0$, the small-angle limit (5) is recovered.

3. Field Observations

Field observations were collected near Duck, North Carolina, on a barrier island exposed to the Atlantic Ocean during the Duck94 (September-October 1994 [e.g., *Elgar et al.*,
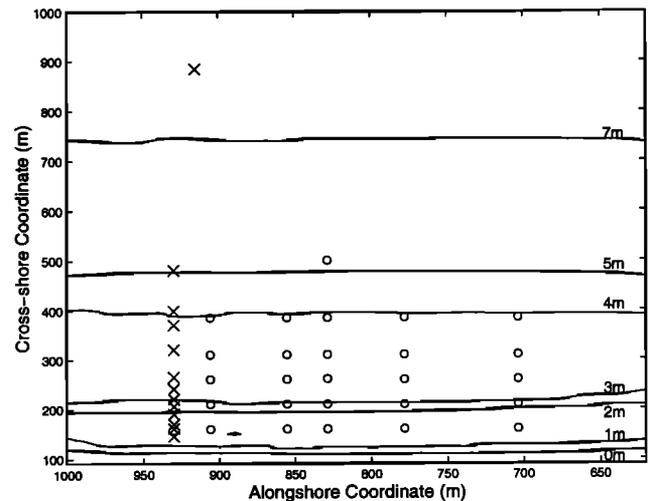
Figure 1. Locations of the 13 Duck94 (crosses) and 26 SandyDuck (circles) current meters used in this study. The U.S. Army Corps of Engineers Field Research Facility (FRF) coordinate system is used. Bathymetry from October 2, 1997, is contoured in units of meters below mean sea level.

Table 1. Statistics of the Velocity Field and the Associated Wave Directional Properties.

	$\bar{v}$, m/s	σ_T, m/s	$\lvert\bar{v}\rvert/\sigma_T$	$\bar{u}/\sigma_T$	σ_v/σ_u	ρ_{uv}	$\bar{\theta}$, deg	σ_θ, deg
Mean	0.03	0.35	0.33	-0.10	0.41	-0.11	-4.7	19.4
Standard Deviation	0.22	0.17	0.30	0.17	0.09	0.19	10.5	3.6
Maximum	1.74	0.96	2.79	1.47	1.21	0.85	44.5	51.7
Minimum	-1.60	0.05	0.00	-1.85	0.21	-0.92	-44.3	9.9

Positive u and v correspond to onshore and southerly flow, respectively.

1997; *Gallagher et al.*, 1998; *Garcez-Faria et al.*, 1998; *Feddersen et al.*, 1998; *Thornton et al.*, 1998; *Herbers et al.*, 1999; and others]) and SandyDuck (August-November 1997 [*Elgar et al.*, 2000]) field experiments. Data used here were acquired from 13 current meters deployed on a cross-shore transect extending 750 m from near the shoreline to 8-m water depth during Duck94 and from a 2-D array of 26 current meters spanning 350 m in the cross-shore and 200 m in the alongshore during SandyDuck (Figure 1). The current meters were raised or lowered as the bed level changed to maintain an elevation between approximately 0.4 to 1.0 m above the seafloor. The sensors closest to shore often were exposed at low tide and therefore inactive. Over all the sensors, the significant wave height ranged from approximately 0.2 to 4 m, the peak wave period from 5 to 12 s, and the wave-directional properties are given in Table 1.

Current meter data acquired at 2 Hz were processed into hourly averaged estimates of $\bar{v}$, $\bar{u}$, σ_u, σ_v, $< \lvert\vec{u}\rvert v >$, and ρ_{uv} resulting in 70,099 estimates of each variable, 15,072 from Duck94 and 55,027 from SandyDuck. The estimated hourly statistics contain contributions from shear and infra-gravity waves, as well as from sea and swell. Velocity statistics (Table 1) show that the assumption of weak-currents ($\lvert\bar{v}\rvert/\sigma_T \ll 1$), small-angles ($\sigma_v/\sigma_u \ll 1$), negligible $\bar{u}$, and unidirectional waves ($\lvert\rho_{uv}\rvert = 1$) used in parameterizations of $< \lvert\vec{u}\rvert v >$ often are violated.

4. Parameterization Tests

4.1. Linear Parameterizations

A linearized parameterization, based on the weak-current and small-angle parameterization (5),

$$< \lvert\vec{u}\rvert v >= a\,\sigma_T \bar{v}, \tag{13}$$

where a is a best fit coefficient, does not describe accurately the observed relationship between $< \lvert\vec{u}\rvert v >$ and $\sigma_T \bar{v}$ (Figure 2a). There is considerable scatter in the observed $< \lvert\vec{u}\rvert v >$ for $\lvert\sigma_T\bar{v}\rvert > 0.2$ m^2/s^2, and a systematic nonlinear trend (e.g., $\lvert < \lvert\vec{u}\rvert v > \rvert$ increases nonlinearly for the largest values of $\lvert\sigma_T\bar{v}\rvert$). The Rayleigh friction form (7) is even less accurate (Figure 2b), with pronounced systematic deviations and a lower skill than (13). With moderately strong flows the errors for both parameterizations (with best fit slopes) are roughly a factor of two. The underprediction of $< \lvert\vec{u}\rvert v >$ is even larger if the weak-current, small-angle value 0.798 is used for a in (13).

The ratio $< \lvert\vec{u}\rvert v > /\sigma_T\bar{v}$ (constant if (13) were correct) depends on $\lvert\bar{v}\rvert/\sigma_T$ (Figure 3). For $\lvert\bar{v}\rvert/\sigma_T > 0.5$, $< \lvert\vec{u}\rvert v > /\sigma_T\bar{v}$ increases approximately linearly with $\lvert\bar{v}\rvert/\sigma_T$, consistent with the expectation that $< \lvert\vec{u}\rvert v > \sim \lvert\bar{v}\rvert\bar{v}$ for strong currents. The linear relationship between $< \lvert\vec{u}\rvert v > /\sigma_T\bar{v}$ and
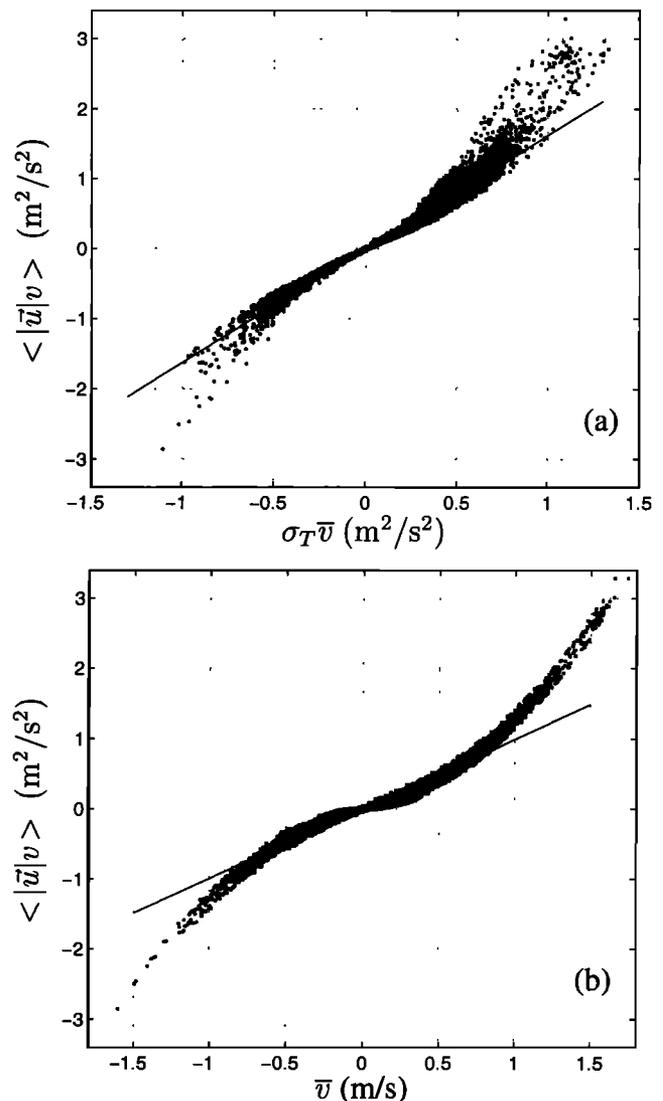
Figure 2. (a) Observed $< \lvert\vec{u}\rvert v >$ versus $\sigma_T\bar{v}$. The solid line is the least squares best fit (slope $a = 1.62$ and skill $r^2 = 0.94$). (b) Observed $< \lvert\vec{u}\rvert v >$ versus $\bar{v}$. The solid line is the least squares best fit (slope = 0.99 m/s and skill $r^2 = 0.88$). Each panel has 70,099 data points.
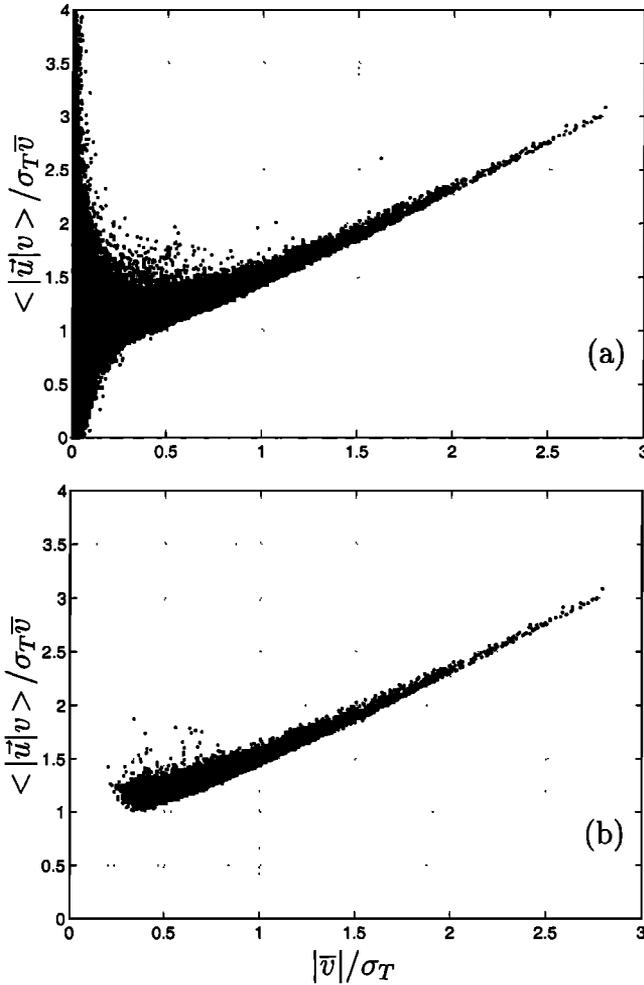
Figure 3. Observed $< |\vec{u}|v > /\sigma_T \bar{v}$ versus $|\bar{v}|/\sigma_T$. (a) All data points in the region $0 < (< |\vec{u}|v > /\sigma_T \bar{v}) < 4$. (b) The subset of data where $| < |\vec{u}|v > | > 0.2$ m^2/s^2 (7857 data points).

$|\bar{v}|/\sigma_T$ is clearer when cases with $| < |\vec{u}|v > | < 0.2$ m^2/s^2 are excluded (Figure 3b). For small values of $|\bar{v}|/\sigma_T$ (i.e., $<$ 0.5), where (13) might be expected to be most accurate, $< |\vec{u}|v > /\sigma_T \bar{v}$ is scattered over a wide range, and many values of $< |\vec{u}|v > /\sigma_T \bar{v}$ are offscale in Figure 3a. As shown below, some of the scatter reflects terms involving the mean cross-shore flow $\bar{u}$ and directional spread that are neglected in the weak-current, small-angle parameterization but are important when $|\bar{v}|/\sigma_T$ is small. Although the relative errors in (13) for small $|\bar{v}|/\sigma_T$ are often large (Figure 3a), the absolute error is small (Figure 2a) because $< |\vec{u}|v >$ usually is small when $|\bar{v}|/\sigma_T \to 0$ (Figure 3b).

4.2. Joint-Gaussian Parameterization

The joint-Gaussian expected value parameterization (12) is accurate, as demonstrated by the close correspondence between observed $< |\vec{u}|v >$ values obtained directly from the velocity time series and $E[|\vec{u}|v]$ using observed values of $\bar{u}$, $\bar{v}$, σ_u, σ_v, and ρ_{uv} (Figure 4a). Although $< |\vec{u}|v > /E[|\vec{u}|v]$ is still scattered for small $|\bar{v}|/\sigma_T$, the scatter for $|\bar{v}|/\sigma_T >$ 0.3 is reduced substantially relative to the linearized parame-

terization (compare Figure 4b with Figure 3a). One possible cause of the remaining scatter in Figure 4b is that for small $|\bar{v}|/\sigma_T$, $E[|\vec{u}|v]/\sigma_T \bar{v}$ is very sensitive to a nonzero skewness (Appendix B), although zero velocity skewness is assumed with a joint-Gaussian velocity field. The velocity skewness usually is nonzero in the surf zone because of nonlinearities in the wave field [*Guza and Thornton*, 1985].

Based on the agreement between $E[|\vec{u}|v]$ and $< |\vec{u}|v >$ (Figure 4a), $E[|\vec{u}|v]$ is used below as a proxy for $< |\vec{u}|v >$ in the surf zone. The dependence of $E[|\vec{u}|v]/\sigma_T \bar{v}$ on $\bar{v}/\sigma_T$, $\bar{u}/\sigma_T$, σ_v/σ_u, and ρ_{uv} are used to explain the distribution of data in Figure 3. The observed ranges of these quantities at Duck (Table 1) are used to guide the parameter space considered and likely are representative of other nearshore environments as well.

The dependence of $E[|\vec{u}|v]/\sigma_T \bar{v}$ on σ_v/σ_u, with $\bar{u} = 0$ and $\rho_{uv} = 0$, is shown in Figure 5a. For $|\bar{v}|/\sigma_T > 0.5$, no
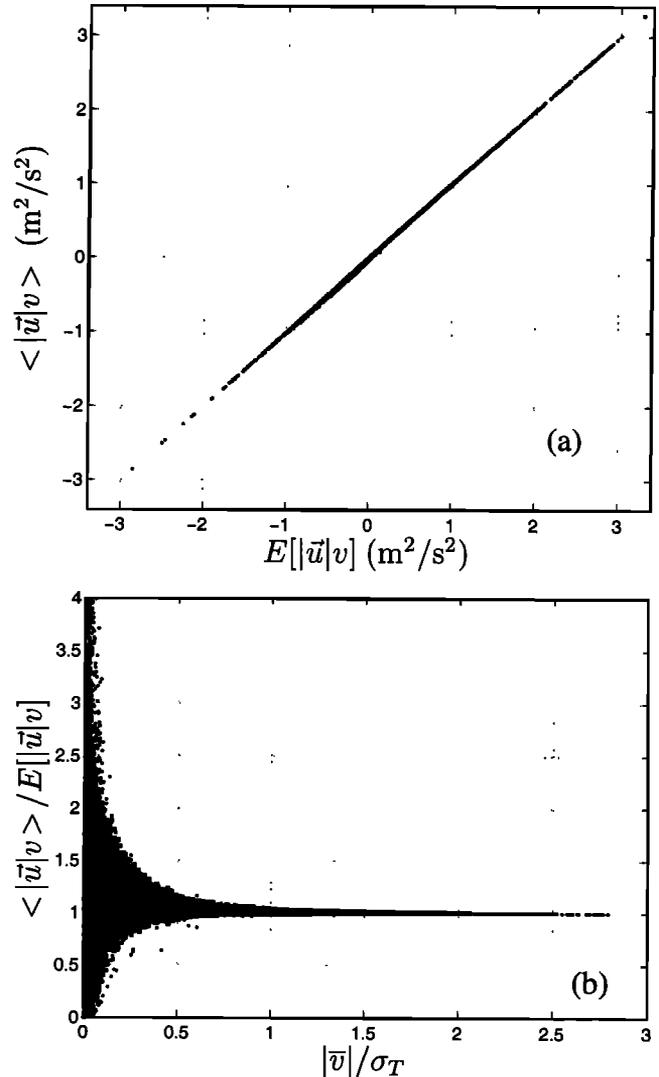
Figure 4. (a) Observed $< |\vec{u}|v >$ versus the expected value $E[|\vec{u}|v]$ assuming a joint-Gaussian velocity field with observed means, variances, and ρ_{uv}. The slope is 1.00, and the skill is $r^2 = 1.00$. (b) The ratio $< |\vec{u}|v > /E[|\vec{u}|v]$ versus $|\bar{v}|/\sigma_T$.
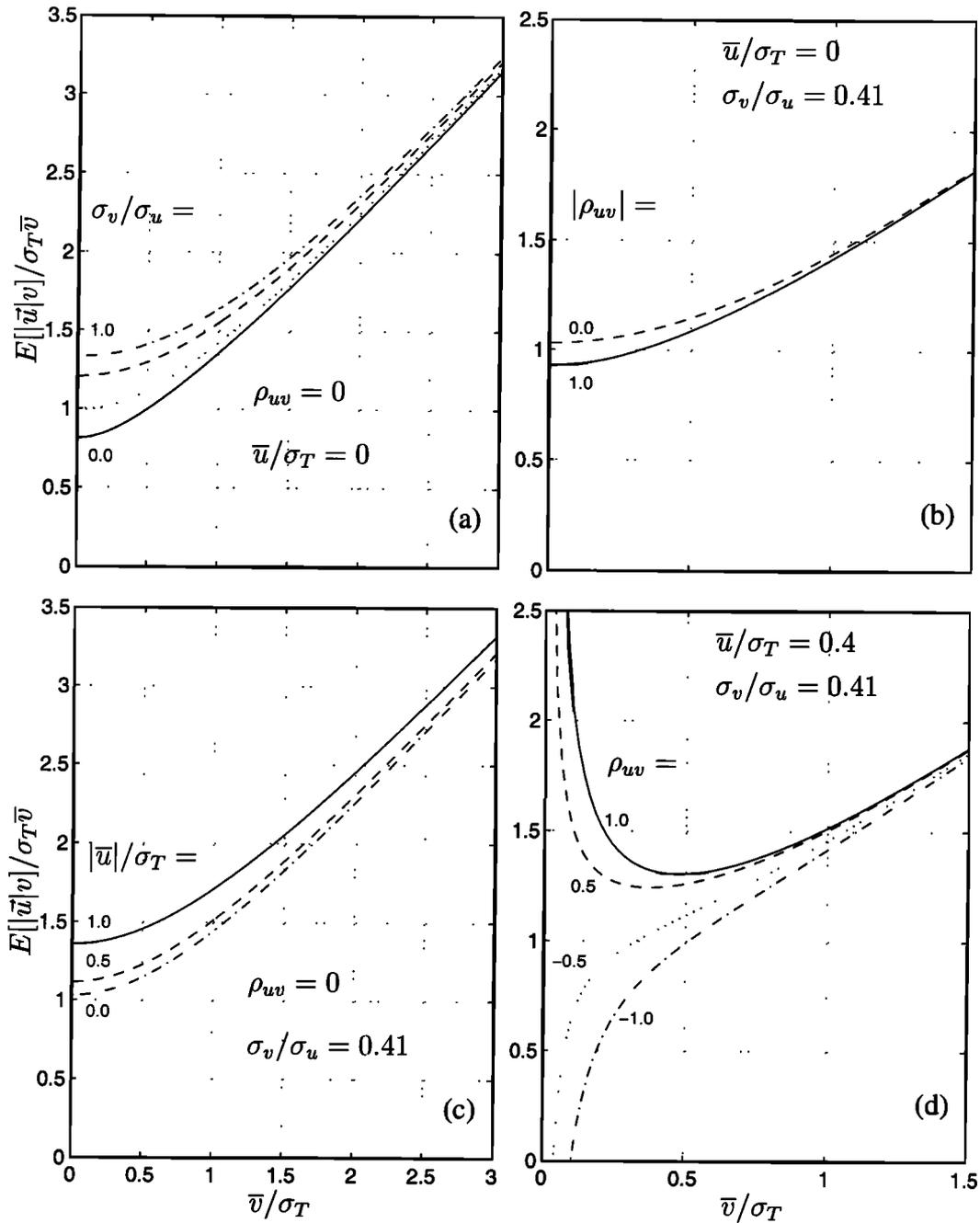
Figure 5. The joint-Gaussian based $E[|\bar{u}|v]/\sigma_T\bar{v}$ versus $|\bar{v}|/\sigma_T$: (a) $\bar{u}/\sigma_u = 0$, $\rho_{uv} = 0$, and $\sigma_v/\sigma_u = 0.0$ (solid), 0.35 (dotted), 0.7 (dashed), and 1.0 (dash-dot). (b) $\bar{u} = 0$, $\sigma_v/\sigma_u = 0.41$ (the observed mean value), and $|\rho_{uv}| = 1.0$ (dashed) and 0 (solid). (c) $\sigma_v/\sigma_u = 0.41$, $\rho_{uv} = 0$, and $|\bar{u}|/\sigma_T = 1.0$ (solid), 0.5 (dashed), and 0 (dash-dot). (d) $\bar{u}/\sigma_T = 0.4$, $\sigma_v/\sigma_u = 0.41$, and $\rho_{uv} = 1.0$ (solid), 0.5 (dashed), -0.5 (dotted), and -1.0 (dash-dot). Note the axes scales of (a) and (c) are different than (b) and (d).

data points in Figure 3a lie below the $\sigma_v/\sigma_u = 0$ curve. The range of $< |\bar{u}|v >/\sigma_T\bar{v}$ with varying σ_v/σ_u decreases with larger $|\bar{v}|/\sigma_T$. The values of $E[|\bar{u}|v]/\sigma_T\bar{v}$ are weakly sensitive to variations of $|\rho_{uv}|$ when $\bar{u}/\sigma_T = 0$ (Figure 5b) and slightly more sensitive to variations of $\bar{u}/\sigma_T$ when $\rho_{uv} = 0$ (Figure 5c). In contrast, when $\bar{u}/\sigma_T \neq 0$ and $\rho_{uv} \neq 0$, $E[|\bar{u}|v]/\sigma_T\bar{v}$ is spread over a wide range of values for small $|\bar{v}|/\sigma_T$ (Figure 5d), and the envelope of the curves roughly

bracket the observed distribution of $< |\bar{u}|v >/\sigma_T\bar{v}$ in Figure 3a. As $|\bar{v}|/\sigma_T \to 0$, $E[|\bar{u}|v]/\sigma_T\bar{v} \to \pm\infty$ because $< |\bar{u}|v >$ does not necessarily vanish when $\bar{v} = 0$, but $\bar{u} \neq 0$ and $\rho_{uv} \neq 0$ (B6). The spreading of $E[|\bar{u}|v]/\sigma_T\bar{v}$ occurs largely for $|\bar{v}|/\sigma_T \leq 0.6$, consistent with the observed spreading of $< |\bar{u}|v >/\sigma_T\bar{v}$ (Figure 3a). As the magnitude of $\bar{u}/\sigma_T$ increases, the spreading of $E[|\bar{u}|v]/\sigma_T\bar{v}$ in Figure 5d persists for larger $|\bar{v}|/\sigma_T$. However, even for relatively ex-
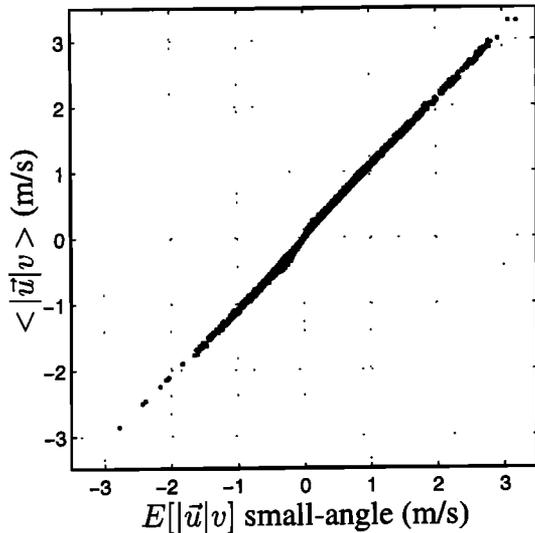
Figure 6. Observed $< |\vec{u}|v >$ versus the closed form small-angle (SA) parameterization (C2) with the observed $\bar{v}$ and σ_T. The best fit slope is 1.06 and the skill $r^2 = 0.98$. The SA parameterization has the poorest fit to $< |\vec{u}|v >$ of all the nonlinear parameterizations (sections 4.3 and 4.4, Table 2) but is still much improved relative to the linear parameterizations (Figure 2).

treme observed values (Table 1) $\bar{u}/\sigma_T = 1$ and $\rho_{uv} = 0.9$, this effect becomes important only for $|\bar{v}|/\sigma_T < 0.75$ (not shown).

4.3. Nonlinear Parameterizations

The ED80, TG86, and $E[|\vec{u}|v]$ for $|\rho_{uv}| = 1$ parameterizations all with $\bar{u} = 0$ (as commonly is assumed in 1-D alongshore current modeling) perform well overall with high skills ($r^2 \geq 0.98$) and best fit slopes close to unity (Table 2) regardless of wave angle definition. With $\bar{u} = 0$, all three parameterizations are functions of three parameters ($\bar{v}$, σ_T, and θ). In ED80 and TG86, $u_0 = \sqrt{2}\sigma_T$ is used. The wave angle θ is set to either the zero spread (i.e., $|\rho_{uv}| = 1$) wave angle $\tan|\theta| = \sigma_v/\sigma_u$, the Kuik et al. [1988] mean wave angle (always closer to normal incidence than the zero spread), or $\theta = 0$. Examining the effect of different wave angles is equivalent to varying σ_v/σ_u. Although the three parameterizations provide a good overall fit to $< |\vec{u}|v >$ (Figure 6), they differ from the full joint-Gaussian $E[|\vec{u}|v]$, particularly as $|\bar{v}|/\sigma_T \rightarrow 0$ (compare Figure 7a with Figures 7b and 7c) where the bias and standard deviations in the ratio of the observed to parameterized $< |\vec{u}|v >$ increase. The bias is greater with $\theta = 0$ than with $\tan|\theta| = \sigma_v/\sigma_u$ (compare Figure 7c with Figure 7b), reflecting the importance of σ_v/σ_u for small $|\bar{v}|/\sigma_T$ (Figure 5a).

Including $\bar{u}$ has a small effect on the skill and best fit slopes of the three parameterizations (not shown) and increases the bias and standard deviations for small $|\bar{v}|/\sigma_T$ (Figure 7d). The performance of these parameterizations is degraded in this case because $|\rho_{uv}| = 1$ is assumed, but $E[|\vec{u}|v]/\sigma_T\bar{v}$ is sensitive to ρ_{uv} for nonzero $\bar{u}/\sigma_T$ and small $|\bar{v}|/\sigma_T$ (Figure 5d). Including nonzero $\bar{u}$ improves the pa-
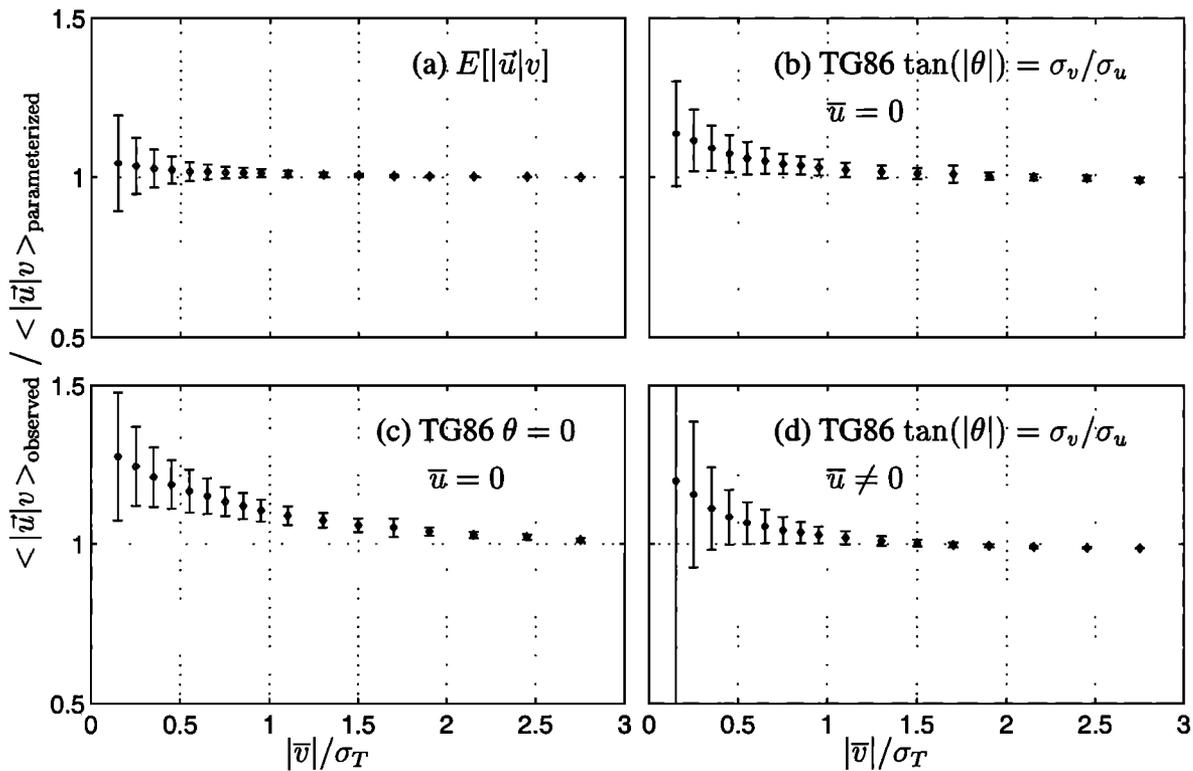
Figure 7. Means (diamonds) and standard deviations (vertical bars) of the ratio of the observed to the parameterized $< |\vec{u}|v >$. (a) The joint-Gaussian $E[|\vec{u}|v]$, (b) TG86 with $\tan(|\theta|) = \sigma_v/\sigma_u$ and $\bar{u} = 0$, (c) TG86 with $\theta = 0$ and $\bar{u} = 0$, and (d) TG86 with $\tan(|\theta|) = \sigma_v/\sigma_u$ and the observed $\bar{u}$.

Table 2. Best fit slopes between the observed $< |\vec{u}|v >$ and TG86, ED80, and $E[|\vec{u}|v]$ with $|\rho_{uv}| = 1$ (all with $\overline{u} = 0$) using three different wave angles.

	TG86	ED80	$E[|\vec{u}|v]$ ($|\rho_{uv}| = 1$)
$\tan |\theta| = \sigma_v/\sigma_u$	1.008	1.013	0.979
$\theta =$ Kuik	1.037	1.044	0.983
$\theta = 0$	1.042	1.050	1.059

The *Kuik et al.* [1988] angle is a principal axes angle calculated from the velocity covariance matrix. The $\theta = 0$ entry for the $E[|\vec{u}|v]$ ($|\rho_{uv}| = 1$) is the SA (C2) parameterization (Figure 6). For all parameterizations the skill $r^2 \geq 0.98$.

rameterizations only if ρ_{uv} is variable as in $E[|\vec{u}|v]$ (Figure 7a). However, the dependence of $E[|\vec{u}|v]/\sigma_T\overline{v}$ on $\overline{u}/\sigma_T$ weakens at moderate $|\overline{v}|/\sigma_T$ (Figures 5c and 5d). The weak $|\overline{v}|/\sigma_T$ cases that contain most of the $< |\vec{u}|v > /\sigma_T\overline{v}$ spreading (Figure 3a) are also the cases of the smallest $| < |\vec{u}|v > |$ (Figure 3b). Therefore the nonlinear parameterizations with either $\overline{u} = 0$ or the observed $\overline{u}$ and $|\rho_{uv}| = 1$ perform well overall (have high skills and best fit slopes close to one, Figure 6).

4.4. Empirical Nonlinear Parameterizations

Empirical parameterizations, hybrids of the weak-current and strong-current forms, are suggested by the distribution of $< |\vec{u}|v > /\sigma_T\overline{v}$ in Figure 3b and attempt to reproduce the $\overline{u} = 0$ behavior of $E[|\vec{u}|v]$ (Figures 5a and 5b) using alge-

braic forms convenient for theoretical and numerical analysis. The *Wright and Thompson* [1983] form (11)

$$< |\vec{u}|v >= \sigma_T\overline{v} \left[\alpha^2 + (|\overline{v}|/\sigma_T)^2\right]^{1/2},$$

is examined with two weak-current limits for α that account for variations of σ_v/σ_u and ρ_{uv} (Figures 5a and 5b). The first $\alpha(\sigma_v/\sigma_u, \rho_{uv})$ is based on a joint-Gaussian wave field and $\overline{u} = 0$ (B4), and is evaluated numerically using the observed σ_v/σ_u and ρ_{uv}. The $\alpha(\sigma_v/\sigma_u, \rho_{uv})$ values typically lie (Table 3) between the small-angle 0.798 and isotropic 1.33 limits. The WT83 form with $\alpha(\sigma_v/\sigma_u, \rho_{uv})$ has best fit slope 1.02, high skill ($r^2 = 0.99$), and low bias for small values of $|\overline{v}|/\sigma_T$ (Figure 8a). This parameterization performs almost as well as the joint-Gaussian based $E[|\vec{u}|v]$ for all values of $|\overline{v}|/\sigma_T$ (compare Figure 8a with Figure 7a).
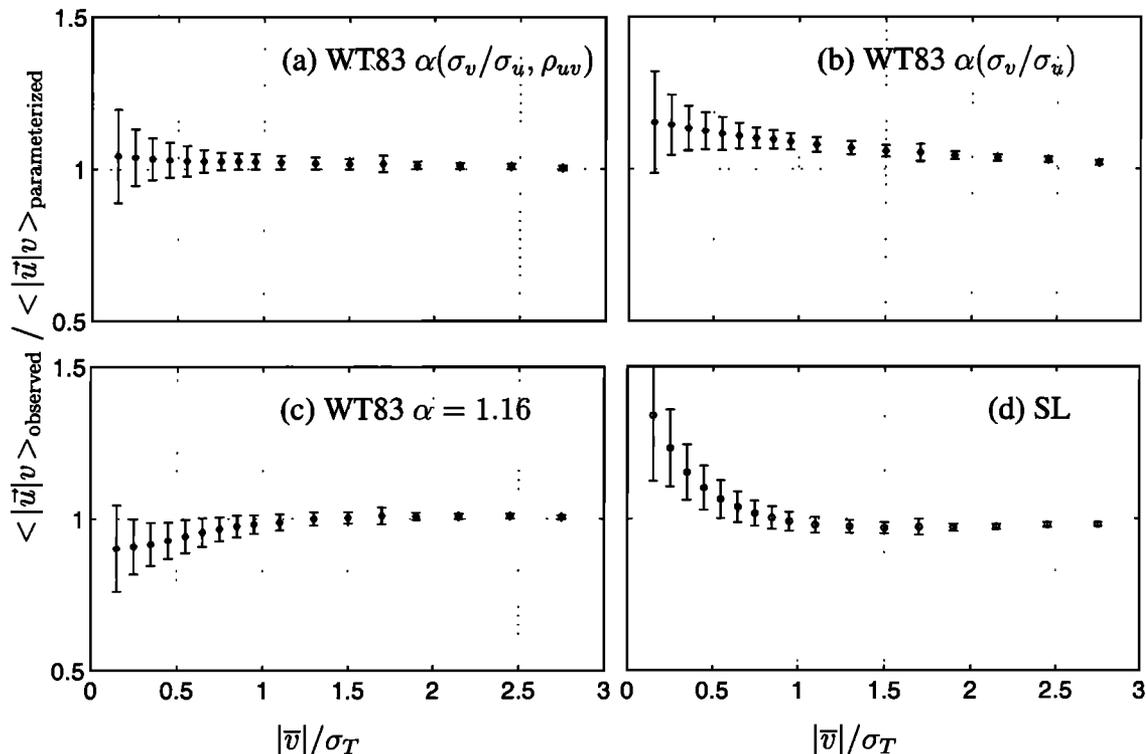
Figure 8. Means (diamonds) and standard deviations (vertical bars) of the ratio of the observed to the parameterized $< |\vec{u}|v >$. (a) WT83 with the weak-current $\alpha(\sigma_v/\sigma_u, \rho_{uv})$, (b) WT83 with the weak-current unidirectional wave $\alpha(\sigma_v/\sigma_u)$, (c) WT83 with the best fit constant $\alpha = 1.16$, and (d) SL with best fit constants $a_1 = 0.66$ and $a_2 = 0.87$.

Table 3. Statistics of $\alpha(\sigma_v/\sigma_u, \rho_{uv})$ (B4) and $\alpha(\sigma_v/\sigma_u)$ (B5) based on the observed σ_v/σ_u and ρ_{uv}.

	Mean	Standard Deviation	Maximum	Minimum
$\alpha(\sigma_v/\sigma_u, \rho_{uv})$	1.02	0.05	1.38	0.88
$\alpha(\sigma_v/\sigma_u)$	0.92	0.04	1.27	0.83

An $\alpha(\sigma_v/\sigma_u)$ based on a unidirectional ($|\rho_{uv}| = 1$) random wave field has a simple closed form expression (B5) that often has smaller values than the more general $\alpha(\sigma_v/\sigma_u, \rho_{uv})$ (Table 3). This is reflected in the increased bias in the ratio of the observed to parameterized $< |\vec{u}|v >$ for small $|\bar{v}|/\sigma_T$ (compare Figure 8b with Figure 8a). However, the best fit slope is 1.05, the skill is high ($r^2 = 0.99$), and the bias and scatter are no larger than the more complicated parameterizations in Figures 7b–7d. Owing to the limited range of both α (Table 3), a best fit constant $\alpha = 1.16$ (that is within the range of weak-current derived α in Table 3) can be used in WT83 (11), with high skill ($r^2 = 0.99$) and only slightly increased bias for small values of $|\bar{v}|/\sigma_T$ (Figure 8c).

A second empirical form, the straight-line parameterization (hereinafter SL),

$$< |\vec{u}|v >= a_1 \sigma_T \bar{v} + a_2 |\bar{v}|\bar{v}, \qquad (14)$$

is suggested by the linear relationship between $< |\vec{u}|v > /\sigma_T\bar{v}$ and $|\bar{v}|/\sigma_T$ in Figure 3b. With the best fit coefficients ($a_1 = 0.66$ and $a_2 = 0.87$) found by fitting (14) to the observed $< |\vec{u}|v >$, SL reproduces $< |\vec{u}|v >$ with high skill ($r^2 = 0.98$). The best fit SL weak-current limit ($a_1 = 0.66$) is smaller than the small-angle limit (0.798), resulting in large bias for small $|\bar{v}|/\sigma_T$ (Figure 8d). However, the errors for $|\bar{v}|/\sigma_T > 0.5$ are similar to the errors for the other nonlinear parameterizations considered. The SL parameterization allows direct solution for $\bar{v}$ in 1-D alongshore current models that balance wave and wind forcing with bottom stress.

These nonlinear $< |\vec{u}|v >$ parameterizations, based on different assumptions of the flow field, have larger errors (Figures 7b–7d and Figure 8) than the joint-Gaussian based $E[|\vec{u}|v]$ (Figure 7a) but may reproduce $< |\vec{u}|v >$ adequately (e.g., Figure 6) for many modeling applications. The critical elements in parameterizing $< |\vec{u}|v >$ accurately are $\bar{v}$ and σ_T. For small $|\bar{v}|/\sigma_T$, other factors (e.g., σ_v/σ_u, $\bar{u}/\sigma_T$, ρ_{uv}, velocity skewness) are also important. The choice of parameterization for a particular application depends on the desired trade-off between complexity and accuracy.

5. Discussion

The $< |\vec{u}|v >$ parameterizations examined above use the observed total velocity variance σ_T^2 that includes variability on timescales of sea and swell (0.05-0.3 Hz) and infragravity and shear waves (< 0.05 Hz). In alongshore current models, σ_T often is inferred from a wave transformation

model [e.g., *Thornton and Guza*, 1983; *Church and Thornton*, 1993; *Lippmann et al.*, 1996] that only includes sea and swell and excludes lower frequency motions. The effect of neglecting infragravity and shear waves in $< |\vec{u}|v >$ parameterizations is investigated here.

During SandyDuck, multiple sensors were deployed at different cross-shore locations (Figure 1). At each of these cross-shore locations, bandpassed σ_u^2 and σ_v^2 were calculated over the sea-swell frequency band and summed to give σ_{Tbp}^2 (the sea-swell bandpassed σ_T). The infragravity contribution to σ_T is largest near the shoreline, where a linear regression between σ_T and σ_{Tbp} yields a best fit slope of 0.83 and $r^2 = 0.94$ (e.g., on average, infragravity and shear waves contribute 17% to σ_T near the shoreline). Farther offshore the infragravity contribution decreases, and the best fit slopes between σ_T and σ_{Tbp} are closer to unity (0.93-0.96) and there is less scatter ($r^2 = 0.98$).

The effect of using a reduced σ_T, σ_{Tr}, in the joint-Gaussian parameterization ($E_r[|\vec{u}|v]$) is examined in Figure 9 by reducing σ_u and σ_v (and therefore σ_T) to 80% of their original values (a typical near-shoreline reduction). For small $|\bar{v}|/\sigma_T$ the $< |\vec{u}|v > /E_r[|\vec{u}|v]$ binned means are about $1/0.8 = 1.25$ (e.g., σ_T/σ_{Tr}), as expected from a weak-current linearization proportional to $\sigma_T\bar{v}$. For larger $|\bar{v}|/\sigma_T$, the $< |\vec{u}|v > /E_r[|\vec{u}|v]$ ratio approaches unity, as expected because both $< |\vec{u}|v >$ and $E_r[|\vec{u}|v] \sim |\bar{v}|\bar{v}$ for large $|\bar{v}|/\sigma_T$. Thus the maximum average underprediction of $< |\vec{u}|v >$, by the factor σ_{Tr}/σ_T, occurs for small $|\bar{v}|/\sigma_T$. Based on the
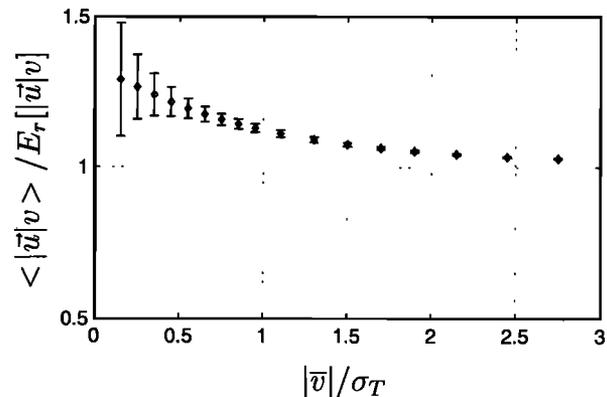
Figure 9. The means (diamonds) and standard deviations (vertical bars) of the ratio $< |\vec{u}|v > /E_r[|\vec{u}|v]$ versus $|\bar{v}|/\sigma_T$. The observed $< |\vec{u}|v >$ is used, and $E_r[|\vec{u}|v]$ is based on the observed $\bar{u}$, $\bar{v}$, and ρ_{uv}, but with 80% of the observed σ_u and σ_v. The corresponding result using the observed σ_u and σ_v is shown in Figure 7a.
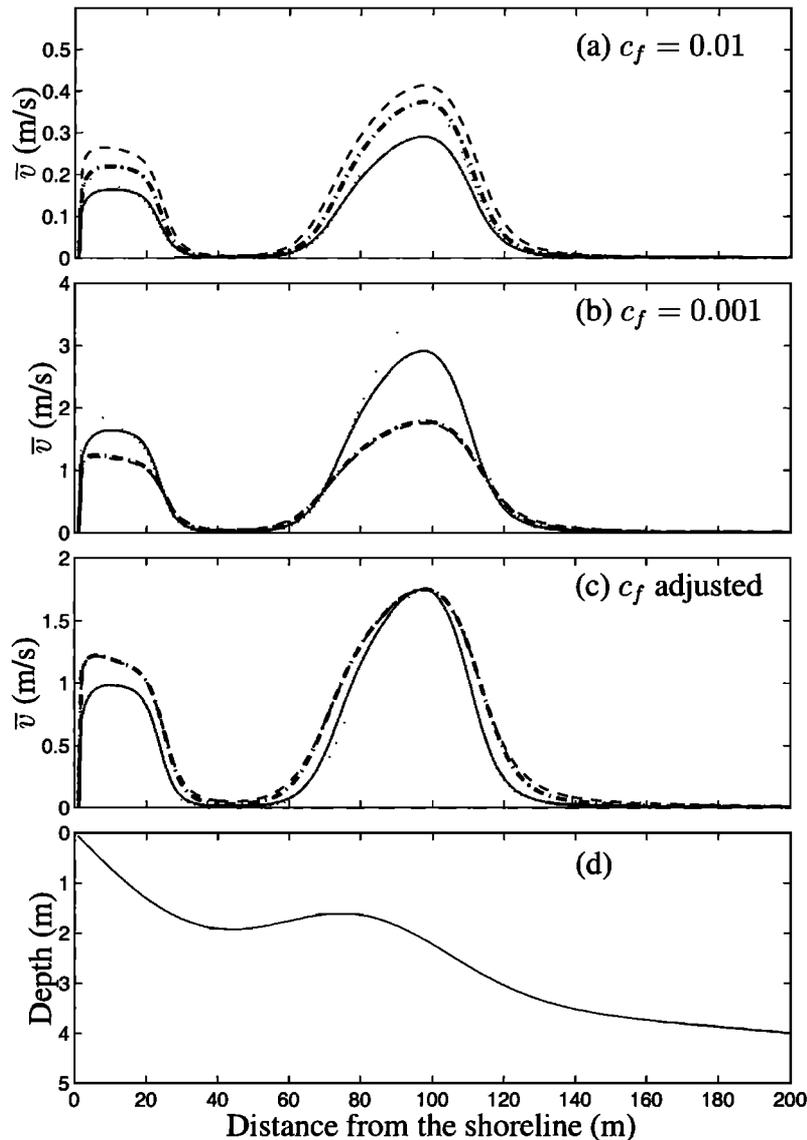
Figure 10. Alongshore current solutions versus distance from the shoreline with four parameterizations for the bottom stress: weak-current (13) (solid curve), Rayleigh (dotted), WT83 (dash-dot), and SL (dashed). Solutions are shown for different values of the drag coefficient c_f: (a) $c_f = 0.01$, (b) $c_f = 0.001$, and (c) with c_f adjusted to yield the same $\bar{v}_{\max}$ as SL with $c_f = 0.001$. The c_f values for the weak-current, Rayleigh, WT83, and SL parameterizations are 1.66, 2.04, 1.03, and 1.00 (all $\times 10^{-3}$), respectively. The flow is forced by waves (offshore $H_{\rm rms} = 1$ m, $\theta = 10°$, and peak period $T = 10$ s) that are transformed using *Church and Thornton* [1993] over the barred bathymetry shown in (d).

best fit slopes between σ_T and $\sigma_{T\rm bp}$, using $\sigma_{T\rm bp}$ results in an average $< |\vec{u}|v >$ error of less than 10% seaward of the shallowest sensor location, and average errors as large as 20% at the shallowest locations, comparable with the mean errors introduced with the nonlinear parameterizations discussed in section 4.3 (compare Figures 7b–7d with Figure 9).

Simple alongshore current models balance the alongshore wave forcing (e.g., gradients in the wave radiation stress) with the alongshore bottom stress τ_y^b. Alongshore current solutions on a barred bathymetry are shown in Figure 10 for four (best fit) $< |\vec{u}|v >$ parameterizations given by

$$\frac{\tau_y^b}{\rho c_f} = \begin{cases} 1.62\,\sigma_T\bar{v} & \text{weak current (13)} \\ 0.99\,\bar{v} & \text{Rayleigh (7)} \\ \sigma_T\bar{v}[1.16^2 + (\bar{v}/\sigma_T)^2]^{1/2} & \text{WT83 (11)} \\ 0.66\,\sigma_T\bar{v} + 0.87\,|\bar{v}|\bar{v} & \text{SL (14),} \end{cases}$$

with c_f constant in the cross-shore. Alongshore current solutions for the first two (linear) models are proportional to c_f^{-1}, whereas the WT83 and SL parameterization have a single solution that scales between $\bar{v} \sim c_f^{-1/2}$ (for stronger forcing) and $\bar{v} \sim c_f^{-1}$ (for weaker forcing). Therefore $\bar{v}$

solutions with SL and WT83 are less sensitive to c_f changes than are solutions with the linear parameterizations.

Garcez-Faria et al. [1998] report a range of drag coefficients $c_f = 0.001$ to $c_f = 0.01$ based on calculating τ_y^b using observed vertical profiles of $\overline{v}$ and bottom boundary layer theory [*Grant and Madsen*, 1979]. For $c_f = 0.01$ (Figure 10a), the maximum $|\overline{v}|/\sigma_T \approx 0.6$, and the magnitude and structure of the four $\overline{v}$ solutions are similar. The small difference between WT83 and SL is consistent with the $|\overline{v}|/\sigma_T \sim 0.5$ trends in Figures 8c and 8d. For $c_f = 0.001$ (Figure 10b), the current is strong (the WT83 and SL maximum $|\overline{v}|/\sigma_T = 2.3$), and the weak-current (13) and Rayleigh (7) parameterization give $\overline{v}_{\max} = 2.9$ m/s and $\overline{v}_{\max} = 3.6$ m/s, respectively, much larger than the $\overline{v}_{\max} = 1.8$ m/s predicted using WT83 or SL. The weak-current $\overline{v}_{\max}$ would be a factor of two greater if the weak-current small angle coefficient 0.798 (5) was used rather than the best fit coefficient 1.62. Similar differences between linear and nonlinear parameterizations are apparent in *Church and Thornton* [1993, Figures 8, 10, and 11], although different c_f values are used for each parameterization. To avoid the unrealistically large velocities predicted with linearized $< |\vec{u}|v >$ parameterizations (Figure 10b), c_f typically is adjusted to match the magnitude of the observed flow (Figure 10c). Although the modeled $\overline{v}(x)$ are all similar, a factor of two adjustment of c_f in the linear parameterizations is needed to match the $\overline{v}_{\max}$ predicted by SL with $c_f = 0.001$, whereas the c_f adjustment is only 3% for WT83. Inferring c_f values by fitting models using linearized bottom stresses to data can be misleading.

6. Conclusions

The weak-current (13) and Rayleigh (7) parameterizations of $< |\vec{u}|v >$ are inaccurate for the wide range of conditions observed between the shoreline and 8-m water depth (Figure 2). The weak-current parameterization has significant bias and scatter at larger $< |\vec{u}|v >$ (Figure 2a). The observed alongshore currents range from weak to strong ($0 < |\overline{v}|/\sigma_T < 3$). The observed distribution of $< |\vec{u}|v > /\sigma_T \overline{v}$ is highly scattered at small $|\overline{v}|/\sigma_T$ and depends linearly on $|\overline{v}|/\sigma_T$ at larger values of $|\overline{v}|/\sigma_T$ (Figure 3) consistent with $< |\vec{u}|v > \sim |\overline{v}|\overline{v}$.

An expected value $E[|\vec{u}|v]$ based on a joint-Gaussian distributed velocity field accurately parameterizes $< |\vec{u}|v >$ (Figure 4a). The observed distribution of $< |\vec{u}|v > /\sigma_T \overline{v}$ (Figure 3a) generally is reproduced by varying the parameters ($\overline{v}/\sigma_T$, $\overline{u}/\sigma_T$, σ_v/σ_u, ρ_{uv}, Appendix B) that govern $E[|\vec{u}|v]/\sigma_T \overline{v}$ (Figure 5).

The joint-Gaussian parameterization $E[|\vec{u}|v]$ requires a more detailed specification of the velocity field than usually is available. Other nonlinear parameterizations, *Ebersole and Dalrymple* [1980], *Thornton and Guza* [1986], and special cases of $E[|\vec{u}|v]$ (A4 and C2), approximately reproduce $< |\vec{u}|v >$ (Table 2 and Figure 6) regardless of the wave angle definition and whether or not the observed $\overline{u}$ is included. The empirical WT83 (11) and the straight-line parameterization (14) also replicate $< |\vec{u}|v >$. The most important factors

in parameterizing $< |\vec{u}|v >$ are $\overline{v}$ and σ_T. At small $|\overline{v}|/\sigma_T$ (< 0.6), other factors (e.g., σ_v/σ_u, $\overline{u}/\sigma_T$, and ρ_{uv}) are also important and the parameterizations differ (Figures 7 and 8). The effect of velocity skewness, not included in any of these parameterizations, may also be important for the weakest flows $|\overline{v}|/\sigma_T < 0.3$.

Neglecting velocity fluctuations in the infragravity frequency band (< 0.05 Hz) on average reduces σ_T by about 20% close to the shoreline, resulting in average errors in the joint-Gaussian values of $E[|\vec{u}|v]$ (Figure 9) comparable with the average errors of the nonlinear parameterizations of section 4.3 (Figures 7b–7d). Errors from neglecting infragravity velocity fluctuations decrease farther offshore. Alongshore current solutions with linear parameterizations of $< |\vec{u}|v >$ are more sensitive to variations in c_f than are solutions using nonlinear parameterizations. Inferring c_f by fitting model solutions using the linear parameterizations to observations can be misleading.

Appendix A: Evaluation of $E[|\vec{u}|v]$

Assuming a joint-Gaussian probability density function for u and v, the expected value of $E[|\vec{u}|v]$ is

$$E[|\vec{u}|v] = \frac{1}{2\pi\sigma_u\sigma_v(1 - \rho_{uv}^2)} \int\!\!\!\int_{-\infty}^{\infty} \sqrt{u^2 + v^2}\, v \times$$
$$\exp\left[-\frac{\sigma_v^2(u-\overline{u})^2 - 2\rho_{uv}\sigma_u\sigma_v(u-\overline{u})(v-\overline{v}) + \sigma_u^2(v-\overline{v})^2}{2\sigma_u^2\sigma_v^2(1 - \rho_{uv}^2)}\right]$$
$$\times du\,dv. \tag{A1}$$

Writing the velocities as mean and fluctuating components (i.e., $u = \overline{u} + u'$) gives

$$E[|\vec{u}|v] = \frac{1}{2\pi\sigma_u\sigma_v(1 - \rho_{uv}^2)} \int\!\!\!\int_{-\infty}^{\infty} \sqrt{(u' + \overline{u})^2 + (v' + \overline{v})^2}$$
$$\times \ (v' + \overline{v})\exp\left(-\frac{1}{2}\mathbf{u}^T\mathbf{C}_{uv}^{-1}\mathbf{u}\right) du'dv'$$

where $\mathbf{u} = [u'\ v']^T$, and the velocity covariance matrix $\mathbf{C}_{uv}$ is

$$\mathbf{C}_{uv} = \begin{bmatrix} \sigma_u^2 & \rho_{uv}\sigma_u\sigma_v \\ \rho_{uv}\sigma_u\sigma_v & \sigma_v^2 \end{bmatrix}. \tag{A2}$$

The symmetric, positive semidefinite matrix $\mathbf{C}_{uv}^{-1}$ exists (because the observed $|\rho_{uv}| \neq 1$ and $\sigma_v \neq 0$) and has an eigenvalue decomposition

$$\mathbf{C}_{uv}^{-1} = \mathbf{L}\mathbf{\Lambda}^{-1}\mathbf{L}^T$$

where $\mathbf{L}$ is the orthonormal eigenvector matrix, and $\mathbf{\Lambda} = \mathrm{diag}(\lambda_i)$ is the eigenvalue matrix. Transforming into the stretched principal axes,

$$\mathbf{x} = \mathbf{\Lambda}^{-1/2}\mathbf{L}^T\mathbf{u}/\sqrt{2},$$

where $\mathbf{x} = [x\ y]^T$, so that

$$\mathbf{x}^T\mathbf{x} = \frac{1}{2}\mathbf{u}^T\mathbf{C}_{uv}^{-1}\mathbf{u}$$

and defining $\mathbf{K} = \sqrt{2}\mathbf{L}\Lambda^{1/2}$, it follows that $\mathbf{u} = \mathbf{Kx}$, and $dudv = \det(\mathbf{K})dxdy$, where $\det(\mathbf{K}) = 2\sqrt{\lambda_1\lambda_2}$.

The term $\sqrt{u^2 + v^2}\, v$ in (A1) is written with the change of variable as ($\mathbf{K} = k_{ij}$),

$$
\begin{aligned}
g(x,y) &= \big[(k_{11}^2 + k_{21}^2)x^2 + 2(k_{11}k_{12} + k_{21}k_{22})xy \\
&\quad + (k_{12}^2 + k_{22}^2)y^2 + 2(k_{11}x + k_{12}y)\bar{u} \\
&\quad + 2(k_{21}x + k_{22}y)\bar{v} + \bar{u}^2 + \bar{v}^2\big]^{1/2} \\
&\quad \times (k_{21}x + k_{22}y + \bar{v}).
\end{aligned}
$$

Defining $\gamma = \pi\sigma_u\sigma_v\sqrt{(1-\rho^2)/(\lambda_1\lambda_2)}$, the integral (A1) becomes

$$
E[|\vec{u}|v] = \frac{1}{\gamma}\iint\limits_{-\infty}^{\infty} g(x,y)\exp[-(x^2 + y^2)]dxdy. \quad \text{(A3)}
$$

Equation (A3) was integrated numerically using a $n = 24$ point quadrature scheme for both x and y appropriate for integrals of the form (A3) [*Abramowitz and Stegun*, 1965],

$$
E[|\vec{u}|v] \approx \frac{1}{\gamma}\sum_{i=1}^{n}\sum_{j=1}^{n} w_{ij}g(x_i, y_j)
$$

where x_i and y_j are the zeros of the Hermite polynomials $H_n(x)$ and $H_n(y)$, and w_{ij} are the weights

$$
w_{ij} = \frac{2^{2n-2}n!n!\pi}{n^4 H_{n-1}^2(x_i)H_{n-1}^2(y_j)}.
$$

This scheme is both accurate and efficient. An $n = 12$ point quadrature scheme also could be used in a circulation model. For the case where $\bar{u} = 0$ and $\sigma_v = 0$ the numerical integration agrees well with the closed form solution (Appendix C) for the small-angle parameterization. Small errors in the numerical integration as $\bar{v}/\sigma_u \to 0$ with $\bar{u} = 0$ are expected because the function $\sqrt{u^2}$ has a discontinuous derivative at $u = 0$. The quadrature scheme is most accurate with functions that are continuous and have continuous derivatives.

If the wave spread σ_θ is assumed zero (i.e., $\rho_{uv} = \pm 1$) as in TG86 and ED80, then the double integral in (A1) is transformed into a single integral

$$
\begin{aligned}
E[|\vec{u}|v] &= \frac{1}{\sqrt{2\pi}\sigma_T}\int_{-\infty}^{\infty} \big[(u_T'\cos(\theta) + \bar{u})^2 + (u_T'\sin(\theta) \\
&\quad + \bar{v})^2\big]^{1/2}(u_T'\sin(\theta) + \bar{v})\exp\left[\frac{-u_T'^2}{2\sigma_T^2}\right]du_T', \text{(A4)}
\end{aligned}
$$

that is calculated readily with an similar quadrature scheme.

Although $< |\vec{u}|u >$ is not related obviously to the time-averaged cross-shore bottom stress because of the strong depth variation in $\bar{u}$, it is interesting to examine whether the relationship between $< |\vec{u}|u >$ and $E[|\vec{u}|u]$ is as robust as that between $< |\vec{u}|v >$ and $E[|\vec{u}|v]$ (Figure 4). The joint-Gaussian $E[|\vec{u}|u]$, integrated numerically with the scheme described above, is compared with $< |\vec{u}|u >$ in Figure A1.
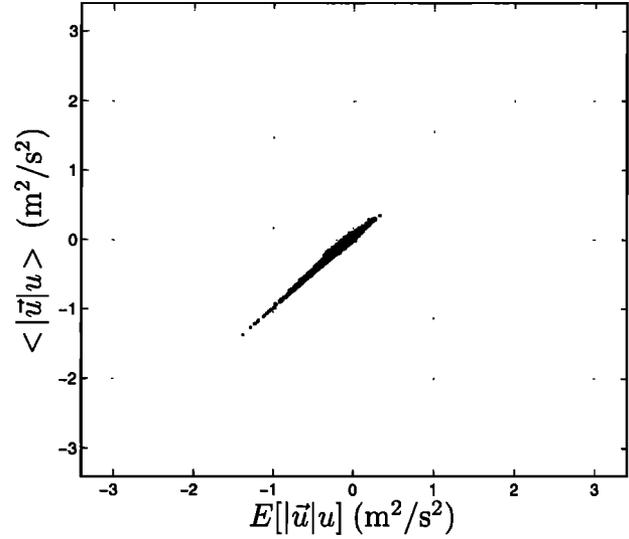
Figure A1. Observed $< |\vec{u}|u >$ versus $E[|\vec{u}|u]$. The skill $r^2 = 0.95$ and $N = 70,099$. The scale is the same as in Figure 4.

The skill between $< |\vec{u}|u >$ and $E[|\vec{u}|u]$ is high ($r^2 = 0.95$) but is lower than that between $< |\vec{u}|v >$ and $E[|\vec{u}|v]$. The reduced range of observed $< |\vec{u}|u >$ and increased scatter at small values of $< |\vec{u}|u >$ relative to $< |\vec{u}|v >$ both contribute to the lower skill.

Appendix B: Weak-current Approximations

For a joint-Gaussian velocity field the ratio $< |\vec{u}|v > /\sigma_T\bar{v}$ (with the change of variable, $x = u'/\sigma_T$ and $y = v'/\sigma_T$) is

$$
\begin{aligned}
\frac{E[|\vec{u}|v]}{\sigma_T\bar{v}} &= \frac{\left(\frac{\sigma_u}{\sigma_v} + \frac{\sigma_v}{\sigma_u}\right)}{2\pi(1-\rho_{uv}^2)}\iint\limits_{-\infty}^{\infty}\left[\left(x+\frac{\bar{u}}{\sigma_T}\right)^2 + \left(y+\frac{\bar{v}}{\sigma_T}\right)^2\right]^{\frac{1}{2}} \\
&\quad \times \left(y\frac{\sigma_T}{\bar{v}} + 1\right) \\
&\quad \times \exp\left[-\frac{x^2\left(1+\frac{\sigma_u^2}{\sigma_u^2}\right) + 2\rho_{uv}xy\left(\frac{\sigma_v}{\sigma_u} + \frac{\sigma_u}{\sigma_v}\right) + y^2\left(1+\frac{\sigma_u^2}{\sigma_v^2}\right)}{2(1-\rho_{uv}^2)}\right] \\
&\quad \times dxdy, \quad \text{(B1)}
\end{aligned}
$$

which is a function of four nondimensional quantities, $\bar{v}/\sigma_T$, $\bar{u}/\sigma_T$, σ_v/σ_u, and ρ_{uv}. Denoting the expected value with the brackets operator, (B1) is

$$
\frac{E[|\vec{u}|v]}{\sigma_T\bar{v}} = \left\langle\left[\left(x+\frac{\bar{u}}{\sigma_T}\right)^2 + \left(y+\frac{\bar{v}}{\sigma_T}\right)^2\right]^{\frac{1}{2}}\left(y\frac{\sigma_T}{\bar{v}}+1\right)\right\rangle. \quad \text{(B2)}
$$

For weak-currents (i.e., small $\bar{v}/\sigma_T$ and $\bar{u}/\sigma_T$), Taylor expanding the square root in (B2) and keeping up to linear terms in the mean current gives

$$
\begin{aligned}
\frac{E[|\vec{u}|v]}{\sigma_T\bar{v}} &= \left\langle (x^2 + y^2)^{1/2}\left[1 + \frac{x}{(x^2+y^2)}\frac{\bar{u}}{\sigma_T}\right.\right. \\
&\quad \left.\left. + \frac{y}{(x^2+y^2)}\frac{\bar{v}}{\sigma_T}\right]\left(y\frac{\sigma_T}{\bar{v}}+1\right)\right\rangle.
\end{aligned}
$$

The joint-Gaussian expected value of odd functions is zero so

$$\left\langle \frac{x}{(x^2+y^2)^{1/2}} \right\rangle \frac{\bar{u}}{\sigma_T} = \left\langle \frac{y}{(x^2+y^2)^{1/2}} \right\rangle \frac{\bar{v}}{\sigma_T} =$$

$$\left\langle y(x^2+y^2)^{1/2} \right\rangle \frac{\sigma_T}{\bar{v}} = 0.$$

Note that if the underlying probability density function has a nonzero skewness, then $< y(x^2+y^2)^{1/2} > \neq 0$, and as $|\bar{v}|/\sigma_T \to 0$, $E[|\vec{u}|v]/\sigma_T\bar{v} \to \pm\infty$.

For weak-currents and a joint-Gaussian velocity field,

$$\frac{E[|\vec{u}|v]}{\sigma_T\bar{v}} = \left\langle (x^2+y^2)^{1/2} + \frac{y^2 + xy\frac{\bar{u}/\sigma_T}{\bar{v}/\sigma_T}}{(x^2+y^2)^{1/2}} \right\rangle. \quad (B3)$$

With the common alongshore current modeling assumption $\bar{u} = 0$, (B3) reduces to a function of σ_v/σ_u and ρ_{uv},

$$\frac{E[|\vec{u}|v]}{\sigma_T\bar{v}} = \left\langle \frac{x^2 + 2y^2}{(x^2+y^2)^{1/2}} \right\rangle, \quad (B4)$$

which can be integrated using techniques described in Appendix A. The isotropic case ($\sigma_v/\sigma_u = 1$ and $\rho_{uv} = 0$) considered by *Wright and Thompson* [1983] is recovered from (B4),

$$\frac{E[|\vec{u}|v]}{\sigma_T\bar{v}} = \frac{3}{4}\Gamma(1/2) = \frac{3\sqrt{\pi}}{4},$$

where Γ is the gamma function. When $|\rho_{uv}| = 1$, $\tan(|\theta|) = \sigma_v/\sigma_u$, and (B4) yields a closed form solution,

$$\frac{E[|\vec{u}|v]}{\sigma_T\bar{v}} = \sqrt{\frac{2}{\pi}}\left[1 + \frac{\sigma_v^2/\sigma_u^2}{1+\sigma_v^2/\sigma_u^2}\right]$$

$$= \sqrt{\frac{2}{\pi}}\left[1 + \sin^2\theta\right]. \quad (B5)$$

The correction for wave obliquity is the same as for unidirectional monochromatic waves (6) [*Liu and Dalrymple*, 1978].

Allowing $\bar{u}/\sigma_T \neq 0$ with $|\rho_{uv}| = 1$ gives a closed form expression for the third term in (B3)

$$\left\langle \frac{xy}{(x^2+y^2)^{1/2}} \right\rangle \frac{\bar{u}/\sigma_T}{\bar{v}/\sigma_T} = \sqrt{\frac{2}{\pi}}\,\text{sgn}(\rho_{uv})\left(\frac{\sigma_u}{\sigma_v} + \frac{\sigma_v}{\sigma_u}\right)^{-1}$$

$$\times\frac{\bar{u}/\sigma_T}{\bar{v}/\sigma_T} = \sqrt{\frac{2}{\pi}}\,\text{sgn}(\rho_{uv})\frac{\sigma_u\sigma_v}{\sigma_T^2}\frac{\bar{u}}{\bar{v}}, \quad (B6)$$

where $\text{sgn}(\rho_{uv})$ is the sign of ρ_{uv}. For $\bar{u} \neq 0$, as $\bar{v} \to 0$ the ratio $E[|\vec{u}|v]/\sigma_T\bar{v} \to \pm\infty$ depending on the signs of $\rho_{uv}, \bar{u}$, and $\bar{v}$. When $\rho_{uv} = 0$,

$$\left\langle \frac{xy}{(x^2+y^2)^{1/2}} \right\rangle = 0,$$

and $\bar{u}$ does not enter into the weak-current forms.

Appendix C: Small-Angle Parameterization

The small-angle (SA) parameterization follows from (A1) with the assumption that alongshore velocities are negligible ($\sigma_v = 0$) and $\bar{u} = 0$,

$$E[|\vec{u}|v] = \frac{\bar{v}}{\sqrt{2\pi}\sigma_T}\int_{-\infty}^{\infty}\sqrt{u'^2 + \bar{v}^2}\exp\left(\frac{-u'^2}{2\sigma_T^2}\right)du'. \quad (C1)$$

Changing variables so $r^2 = u'^2/(2\sigma_T^2)$ and $b = \bar{v}^2/(4\sigma_T^2)$ yields

$$E[|\vec{u}|v] = \sqrt{\frac{2}{\pi}}\sigma_T\bar{v}\cdot\int_{-\infty}^{\infty}\sqrt{r^2 + 2b}\cdot\exp(-r^2)dr$$

$$= \sqrt{\frac{2}{\pi}}\sigma_T\bar{v}\cdot b\exp(b)\left[K_0(b) + K_1(b)\right] \quad (C2)$$

where K_0 and K_1 are the modified Bessel functions of the second kind. As $|\bar{v}|/\sigma_T \to 0$, $b \to 0$, $\exp(b) \sim 1 + b$, $K_0(b) \sim -\ln b$, and $K_1(b) \sim b^{-1}$, so to leading order

$$E[|\vec{u}|v] \sim \sqrt{\frac{2}{\pi}}\sigma_T\bar{v}\cdot b(1+b)(b^{-1} - \ln b) \sim \sqrt{\frac{2}{\pi}}\sigma_T\bar{v},$$

recovering the weak-current limit. As $|\bar{v}|/\sigma_T \to \infty$, $b \to \infty$,

$$K_0(b), K_1(b) \sim \sqrt{\pi/2}\,b^{-1/2}\exp(-b)$$

so to leading order

$$E[|\vec{u}|v] \sim \sqrt{\frac{2}{\pi}}\sigma_T\bar{v}\cdot 2\sqrt{\frac{\pi}{2}\frac{\bar{v}}{2\sigma_T}} = |\bar{v}|\bar{v}$$

recovering the strong-current limit.

References

Abramowitz, M., and I. Stegun, *Handbook of Mathematical Functions*, Dover, New York, 1965.

Allen, J. S., P. A. Newberger, and R. A. Holman, Nonlinear shear instabilities of alongshore currents on plane beaches, *J. Fluid Mech.*, *310*, 181–213, 1996.

Battjes, J. A., Surf-zone dynamics, *Ann. Rev. Fluid Mech.*, *20*, 257–293, 1988.

Bowden, K. F., Note on wind drift in a channel in the presence of tidal currents, *Proc. R. Soc. London A*, *219*, 426–446, 1953.

Bowen, A.J., The generation of longshore currents on a plane beach, *J. Mar. Res.*, *27*, 206–215, 1969.

Church, J. C., and E. B. Thornton, Effects of breaking wave induced turbulence within a longshore current model, *Coastal Eng.*, *20*, 1–28, 1993.

Dodd, N., J. Oltman-Shay, and E. B. Thornton, Shear instabilities in the longshore current: A comparison of observation and theory, *J. Phys. Oceanogr.*, *22*, 62–82, 1992.

Ebersole, B. A. and R. A. Dalrymple, Numerical modeling of nearshore circulation, in *Proc. 17th Int. Coastal Engineering Conf.*, pp. 2710–2725, Am. Soc. Civ. Eng., New York, 1980.

Elgar, S., R. T. Guza, B. Raubenheimer, T. H. C. Herbers, and E. Gallagher, Spectral evolution of shoaling and breaking waves on a barred beach, *J. Geophys. Res.*, *102*, 15,797–15,805, 1997.

Elgar, S., R. T. Guza, W. C. O'Reilly, B. Raubenheimer, and T. H. C. Herbers, Observations of wave energy and direction near a pier, *J. Waterw. Port Coastal Ocean Eng.*, in press, 2000.

Feddersen, F., Finite amplitude shear waves, *J. Fluid Mech.*, *372*, 71–91, 1998.

Feddersen, F., R. T. Guza, S. Elgar, and T. H. C. Herbers, Alongshore momentum balances in the nearshore, *J. Geophys. Res.*, *103*, 15,667–15,676, 1998.

Gallagher, E. L., S. Elgar, and R. T. Guza, Observations of sand bar evolution on a natural beach, *J. Geophys. Res.*, *103*, 3203–3215, 1998.

Garcez-Faria, A. F., E. B. Thornton, T. P. Stanton, C. V. Soares, and T. C. Lippmann, Vertical profiles of longshore currents and related bed shear stress and bottom roughness, *J. Geophys. Res.*, *103*, 3217–3232, 1998.

Grant, W. D., and O. S. Madsen, Combined wave and current interaction with a rough bottom, *J. Geophys. Res.*, *84*, 1797–1808, 1979.

Guza, R. T., and E. B. Thornton, Velocity moments in the nearshore, *J. Waterw. Port Coastal Ocean Eng.*, *111*, 235–256, 1985.

Herbers, T. H. C., S. Elgar, and R. T. Guza, Directional spreading of waves in the nearshore, *J. Geophys. Res.*, *104*, 7683–7693, 1999.

Kuik, A. J., G. P. van Vledder, and L. H. Holthuijsen, A method for the routine analysis of pitch-and-roll buoy wave data, *J. Phys. Oceanogr.*, *18*, 1020–1034, 1988.

Lentz, S. J., and C. D. Winant, Subinertial currents on the southern California shelf, *J. Phys. Oceanogr.*, *16*, 1737–1750, 1986.

Lentz, S. J., R. T. Guza, S. Elgar, F. Feddersen, and T. H. C. Herbers, Momentum balances on the North Carolina inner shelf, *J. Geophys. Res.*, *104*, 18,205–18,226, 1999.

Lippmann, T. C., A. H. Brookins, and E. B. Thornton, Wave energy transformation on natural profiles, *Coastal. Eng.*, *27*, 1–20, 1996.

Liu, P. L., and R. A. Dalrymple, Bottom frictional stresses and longshore currents due to waves with large angles of incidence, *J. Mar. Res.*, *36*, 357–373, 1978.

Longuet-Higgins, M. S., On the statistical distribution of the heights of sea waves, *J. Mar. Res.*, *11*, 245–266, 1952.

Longuet-Higgins, M. S., Longshore currents generated by obliquely incident sea waves, 1, *J. Geophys. Res.*, *75*, 6790–6801, 1970.

Özkan-Haller, H. T., and J. T. Kirby, Nonlinear evolution of shear instabilities of the longshore current: A comparison of observations and computations, *J. Geophys. Res.*, *104*, 25,953–25,984, 1999.

Rooth, C., A linearized bottom friction law for large-scale oceanic motions, *J. Phys. Oceanogr.*, *2*, 509–510, 1972.

Slinn, D. N., J. S. Allen, P. A. Newberger, and R. A. Holman, Nonlinear shear instabilities of alongshore currents over barred beaches, *J. Geophys. Res.*, *103*, 18,357–18,379, 1998.

Thornton, E. B., Variation of longshore current across the surf zone, in *Proc. 12th Int. Coastal Engineering Conf.*, pp. 291–308, Am. Soc. of Civ. Eng., New York, 1970.

Thornton, E. B., and R. T. Guza, Transformations of wave height distribution, *J. Geophys. Res.*, *88*, 5925–5938, 1983.

Thornton, E. B., and R. T. Guza, Surf zone longshore currents and random waves: Field data and models, *J. Phys. Oceanogr.*, *16*, 1165–1178, 1986.

Thornton, E. B., J. L. Swayne, and J. R. Dingler, Small-scale morphology across the surf zone, *Mar. Geol.*, *145*, 173–196, 1998.

Wright, D. G., and K. R. Thompson, Time-averaged forms of the nonlinear stress law, *J. Phys. Oceanogr.*, *13*, 341–346, 1983.

Wu, C. S., E. B. Thornton, and R. T. Guza, Waves and longshore currents: Comparison of a numerical model with field data, *J. Geophys. Res.*, *90*, 4951–4958, 1985.

S. Elgar, Woods Hole Oceanographic Institution, Woods Hole, MA, 02543. (e-mail: elgar@whoi.edu)

F. Feddersen and R.T. Guza, Center for Coastal Studies Scripps Institution of Oceanography, University of California, La Jolla, CA 92093-0209. (e-mail:falk@coast.ucsd.edu; rguza@ucsd.edu)

T.H.C. Herbers, Deptartment of Oceanography, Naval Postgraduate School, Monterey, CA 93943-5122 (e-mail: herbers@zee.oc.nps.navy.mil)